Half-metallic CrAs nanosheet for magnetic tunnel junctions

Qiang Lu,[1] Wei-Jiang Gong,[2] Sean Li,[3] Xiao-Tao Zu,[1] and Hai-Feng Lü[1,*]

[1]*School of Physics, University of Electronic Science and Technology of China, Chengdu 611731, China*
[2]*College of Sciences, Northeastern University, Shenyang 110819, China*
[3]*School of Materials Science and Engineering, The University of New South Wales, Australia*

The research of magnetic tunnel junctions (MTJs) has scientific and technical significance for promoting the development of information storage technology, promoting spintronics and realizing higher-density integrated circuits. At present, mainly by improving the material and designing alternative structures, the performance and reliability of the MTJs can be enhanced. Recently, it has been reported that the monolayer CrAs is expected to be a ferromagnetic half-metal with high Curie temperature. Here, using DFT+U, we investigate the magnetic and spin-dependent transport properties in a MTJ made of half-metallic CrAs nanosheet. The magnetic anisotropy energy (MAE) along the z axis is $637 \, \mu$eV per Cr, and the ferromagnetism and out-of-plane easy magnetization are not affected by biaxial strain. In addition, the spin-dependent transport features of two MTJs with arsenene inserted in the CrAs layer were theoretically developed and investigated. The findings reveal that tunneling magnetoresistance ratio peaks at approximately equal to 10^{10} and remains more than approximately equal to 10^6 even when subjected to bias voltages as high as 1 V. Moreover, 100% spin-filtering effects can be observed in the devices. Our research offers viable MTJs possibilities for the next spintronic devices.

I. INTRODUCTION

As electronic devices undergo ongoing miniaturization, with some even reaching nanoscale dimensions, the significance of quantum confinement effects becomes increasingly pronounced in the performance of nanodevices. Spintronics, a pioneering branch of electronics, explores the interplay between charge and spin transport [1–4]. It harnesses the intrinsic spin property of electrons to facilitate the storage, transmission, and retrieval of data. For spintronic devices, such as spin field-effect transistors [5–8], spin valves [9–13], and spin filters, to function properly [14–18], large spin currents must be transferred from a magnet to a semiconductor in an efficient manner. Among the crucial spintronic devices, magnetic tunneling junctions (MTJs) find extensive application in various technological domains, including magnetic storage, magnetic sensors, and magnetic logic devices [19–23]. Their primary goal is to achieve the a maximum feasible spin polarization ratio (SPR) and tunneling magnetoresistance (TMR) for use in practical applications, requiring significant sensitivity [24–28]. Using an external magnetic field, the ferromagnetic electrodes may be configured in parallel configuration (PC) or antiparallel configuration (APC), modulating the MTJs' electrical resistance. This

causes the tunneling currents in these two configurations to vary, which causes the TMR phenomenon to occur [29,30]. Thus, the ideal materials to use for MTJ devices are half-metallic magnetic materials, which have a metallic majority spin and a semiconductivity minority spin. They create MTJs with high TMR ratios and provide currents that are 100% spin polarized.

The inherent magnetic characteristics are absent in the majority of the currently available pure two-dimensional (2D) materials, including graphene, phosphorene, and transition-metal dichalcogenides (TMDs) [31–37]. Nanodevices with high performance may be created by structurally modifying and combining these 2D materials [38–40]. But this introduced magnetism is weak and sensitive, has poor controllability, and is difficult to achieve experimentally. Following the 2017 finding of inherent ferromagnetism in monolayer CrI$_3$ and Cr$_2$Gr$_2$Te$_6$, 2D magnetic materials research has recently gained popularity [41–45]. Common ferromagnetic (FM) materials include CrBr$_3$, CrTe, FeTe (hexagonal phase), CrSe, etc. However, Curie temperature (T_C) for the majority of them is quite low (30 K for the Cr$_2$Gr$_2$Te$_6$ bilayer and 45 K for the CrI$_3$ monolayer). The low T_C of these materials significantly impedes their practical usage in spintronics. Compared to other 2D magnetic materials, transition metal sulfides have a relatively high magnetic transition temperature, such as the T_C of Cr$_2$S$_3$ near room temperature [46]. 2D

---

*Contact author: lvhf04@uestc.edu.cn

half-metallic magnetic materials are of great significance in spintronics due to their unusual electronic structure. Therefore, combining high T_C with significant spin polarization, 2D intrinsic half-metallic magnetic materials are of particular interest and significance.

Recently, Zhang *et al.* discovered that Mn_2NF_2 exhibits a suitable FM ground state with a gapless spin-up band, wide gap in spin-down band, and the T_C is much higher than room temperature. The $Mn_2NF_2/Ti_2CO_2/Mn_2NF_2$ MTJ shows a TMR effect of as high as $10^9\%$ [47]. In their theoretical estimation, Ma and colleagues predicted that 2D Janus Mn_2PSb and Mn_2AsSb nanosheets with high T_C of 334 and 385 K, respectively, would include a stable inherent half-metallic FM [48]. In the same way, V_3F_8 nanosheets have inherent half-metallic FM that are thermally stable at room temperature, according to first-principles calculations by Xiao *et al.* [49]. The half-metallic materials NiOBr and NiOCl also had FM ordering and T_C values of 692 and 671 K [50].

Motivated by the above discussion, recently reported 2D half-metallic CrAs is expected to be the ideal material in spintronics [51]. Monolayer CrAs is shown to be both thermally and dynamically stable and have a high T_C with an out-of-plane magnetization. Furthermore, out-of-plane magnetic MAE and FM coupling can be improved by tensile strain. In addition, we construct CrAs/arsenene/CrAs MTJs and use the nonequilibrium Green's function (NEGF) method to investigate their spin-dependent transport properties. The calculated TMR ratios of MTJs reach up to 10^{10}, and the 100% spin-polarization current can be obtained, indicating that they show outstanding promise as high-performance spintronic device candidates.

II. MODEL AND THEORY

The Vienna *ab initio* simulation package (VASP) utilizes density-functional theory (DFT) for calculating the optimization of the CrAs monolayer [52]. Electron-ion interactions are simulated using the projector augmented-wave (PAW) pseudopotential [53]. The generalized gradient approximation (GGA) is commonly utilized to represent the potential and energy associated with electron exchange-correlation [54]. The maximal atomic force and total energy tolerances for the structural relaxation are within 1.0×10^{-8} eV and 0.01 eV/Å, respectively. Additionally, a $20 \times 20 \times 1 k$ mesh is used, and 520 eV is the kinetic energy cutoff. To avoid boundary-condition effects along the z direction, a vacuum slab of 15 Å is applied. The DFT+U approach is used to apply the effective onsite Coulomb repulsion to the d orbitals of Cr atoms, therefore capturing the impact of robust electronic correlations. $U = 3$ eV is used since that is the value that has been published for monolayer structures based on Cr [55]. Thermal stability is predicted using *ab initio* molecular dynamic

simulation (AIMD) and a Nose-Hoover thermostat scheme for temperature regulation.

We analyze quantum transport characteristics in the MTJs by combining the DFT and NEGF using the Nanodcal package [56,57]. This procedure uses the double-ζ basis to extend wave functions and the GGA level to define the exchange-correlation potential. In k space, the Monkhorst-Pack technique uses $100 \times 1 \times 1$ mesh points to sample the Brillouin zone. With a cutoff energy of 150 hartree, the Fermi distribution function has a temperature of 100 K.

The net current across such MTJs could be represented using quantum transport theory established in recent years, i.e.,

$$I_\sigma = \frac{e}{h} \int T_\sigma(E)[f_L(E) - f_R(E)]\, dE. \tag{1}$$

$T_\sigma(E)$ represents the transmission function across the MTJs with $\sigma = \uparrow, \downarrow$ being the spin index. f_α ($\alpha = L, R$) is the Fermi-Dirac distribution function of lead α. Calculating the transmission function is possible via the following equation [58]:

$$T_\sigma(E) = \mathrm{Tr}[\Gamma_L(E)G^r(E)\Gamma_R(E)G^a(E)]_{\sigma\sigma}, \tag{2}$$

In this equation, $G^r(E)$ and $G^a(E)$ are retarded and advanced Green's functions of this system. Γ_α is the linewidth function used to describe the coupling scattering region and lead α.

It is thus possible to provide the charge current as

$$\begin{aligned} I^P &= I_\uparrow^P + I_\downarrow^P, \\ I^{AP} &= I_\uparrow^{AP} + I_\downarrow^{AP}, \end{aligned} \tag{3}$$

where $I_{\uparrow(\downarrow)}^P$ and $I_{\uparrow(\downarrow)}^{AP}$ are the corresponding currents calculated from Eq. (1). These findings allow for the definition of the TMR [59]:

$$R_{\mathrm{TMR}} = \frac{I^P - I^{AP}}{I^{AP}}. \tag{4}$$

Additionally, the SPR is described as

$$\begin{aligned} R_{\mathrm{SP}}^P &= \frac{I_\uparrow^P - I_\downarrow^P}{I_\uparrow^P + I_\downarrow^P}, \\ R_{\mathrm{SP}}^{AP} &= \frac{I_\uparrow^{AP} - I_\downarrow^{AP}}{I_\uparrow^{AP} + I_\downarrow^{AP}}. \end{aligned} \tag{5}$$

The transport characteristics of these MTJs are also known to follow the Landauer-Büttiker formula under low-bias

voltage [60]:

$$\mathcal{G} = \frac{e^2}{h} T(E_F). \tag{6}$$

$\mathcal{G}$ is the linear conductance with $T(E_F) = \sum_\sigma T_\sigma(E_F)$, and E_F is the system's Fermi level at equilibrium where $V_b = 0$. Following that, the TMR and SPR can be simplified in this situation,

$$R_{\text{TMR}} = \frac{T^P(E_F) - T^{AP}(E_F)}{T^{AP}(E_F)}, \tag{7}$$

$$R_{\text{SP}}^P = \frac{T_\uparrow^P(E_F) - T_\downarrow^P(E_F)}{T_\uparrow^P(E_F) + T_\downarrow^P(E_F)}, \tag{8}$$

$$R_{\text{SP}}^{AP} = \frac{T_\uparrow^{AP}(E_F) - T_\downarrow^{AP}(E_F)}{T_\uparrow^{AP}(E_F) + T_\downarrow^{AP}(E_F)}. \tag{9}$$

III. RESULTS AND DISCUSSIONS

As shown in Fig. 1(a), the CrAs monolayer possesses hexagonal symmetry belonging to the space group of $P3m1$ (No. 156). After optimization, the lattice parameter for the hexagonal unit cell (u.c.) indicated by black lines was determined to be 4.23 Å. Prior to analyzing the electronic band structures of the lattice, it is essential to verify its dynamical and thermal stability. Thus, the force constants were obtained by the use of density-functional perturbation theory in the VASP. Next, we computed the phonon-dispersion spectrum using the PHONOPY program [61]. The phonon spectrum in Fig. 1(b) is devoid of imaginary frequencies, suggesting the dynamic stability of the CrAs nanosheet. Evaluation of the cohesive energy E_C is performed as

$$E_C = E_{\text{CrAs}} - E_{\text{As}} - E_{\text{Cr}}. \tag{10}$$

where $E_{\text{CrAs}}, E_{\text{As}},$ and E_{Cr} are the total energy of CrAs u.c., one As atom and Cr atom. The exothermic nature of the CrAs creation is indicated by the negative E_C value (-3.6 eV per u.c.), indicating that the CrAs monolayer may be synthesized experimentally. To investigate the thermal stability of 2D CrAs, we used AIMD calculations via a $4 \times 4 \times 1$ supercell. As shown in Fig. 1(c), after 5 ps at 300 K, the absence of bond breakup or geometric alteration in the final states during thermal initiation indicates that 2D CrAs remains thermally stable at room temperature.

Then, through the analysis of CrAs total energies with different linear magnetic ordering with DFT+U, we investigated the magnetic ground states. The spin configurations of AFM are shown in Fig. 1(a). The energy difference between the AFM and FM states ($\Delta E = E_{\text{AFM}} - E_{\text{FM}}$) in Fig. 2(a) indicates that the CrAs system has a FM ground state under equilibrium structure. Figure 2(b) shows the

electronic band structure of the CrAs monolayer under the FM state. The CrAs monolayer displays half-metallic properties under FM state: semiconducting in the spin-down channel and metallic in the spin-up channel, and the gap of spin-down band is 3.32 eV. The half-metallicity of the systems allows for long-range spin-polarized currents and 100% spin polarization, making them suitable as spin injection. Figure 2(b) also displays the projected DOS (PDOS) that was estimated for the spin-polarized case. It is evident that the CrAs monolayer is a true half-metal ferromagnet. The specific kind of magnetic phase transition is dictated by the magnetocrystalline direction in 2D hexagonal symmetric systems. One may have a long-range FM phase from the out-of-plane one. Even if an external magnetic field may control the magnetocrystalline orientation of 2D materials, an extremely strong magnetic field may be required. MAE can be used for measuring the inherent magnetic anisotropy of CrAs. MAE is defined as the energy difference ($E_x - E_z$), where E_x/E_z is the energy per u.c. when the magnetization is along the x and z direction. A negative or positive MAE indicates an in-plane or out-of-plane direction, respectively. Figure 2(c) shows that the estimated MAE is 637 μeV, implying that the intrinsic easy axis of CrAs is out of plane. In addition, the impact of biaxial strain upon the magnetism of monolayer CrAs is also discussed. It can be found that strain does not change the ferromagnetism and out of plane easily magnetized properties of 2D CrAs. MAE increases with the increase of stretching degree, while MAE decreases with the increase of compression degree. In the context of the Heisenberg model, the spin Hamiltonian can be estimated using the following expression:

$$H = -J \sum_{i,j} S_i \cdot S_j - A \sum_i (S_i^z)^2. \tag{11}$$

where $J, S,$ and A are the nearest exchange parameter, spin quantum number, and MAE, respectively. The energies of the FM and AFM using a rectangular supercell:

$$E_{\text{AFM}} = E_0 + 2JS^2 - 2AS^2, \tag{12}$$

$$E_{\text{FM}} = E_0 - 6JS^2 - 2AS^2, \tag{13}$$

where E_0 indicates the total energy of system in absence of magnetic coupling. The corresponding J can be represented as follows:

$$J = \frac{E_{\text{AFM}} - E_{\text{FM}}}{8S^2}. \tag{14}$$

The averaged net magnetic moment and specific heat capacity per Cr as a function of temperature are shown in Fig. 2(d). With a calculated $J = 35.21$ meV, the T_C of monolayer CrAs is estimated to be 953 K, indicating that it is able to spontaneously magnetize at temperatures
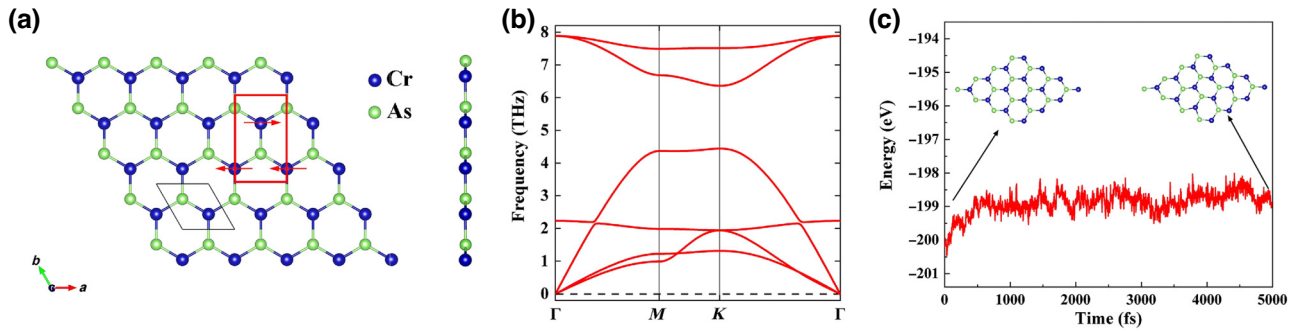
(a)

(b)

(c)

FIG. 1.   (a) Structure diagram of the 2D CrAs. Black (red) lines indicate the primitive (rectangle supercell) cell, and arrows indicate the Cr atoms' spin orientation in the AFM configuration. (b) The calculated phonon dispersion for the 2D AsCr. (c) AIMD of CrAs at 300 K.

well above room temperature. Notably, the predicted T_C of CrAs is an order of magnitude higher than that of CrI$_3$ [45]. The main reason for the high T_C in CrAs is the strong exchange interaction and the large magnetic anisotropy.

Given that substrates will inevitably be used in device applications, the key question is whether the physical features of monolayer CrAs can persist on a substrate. One approach to creating the CrAs nanosheet might be to chemically remove its outer layer from its original bulk crystal, and then place it on a plastic substrate. This method is comparable to the one used to prepare MXenes in experiments. The inherent band character cannot be
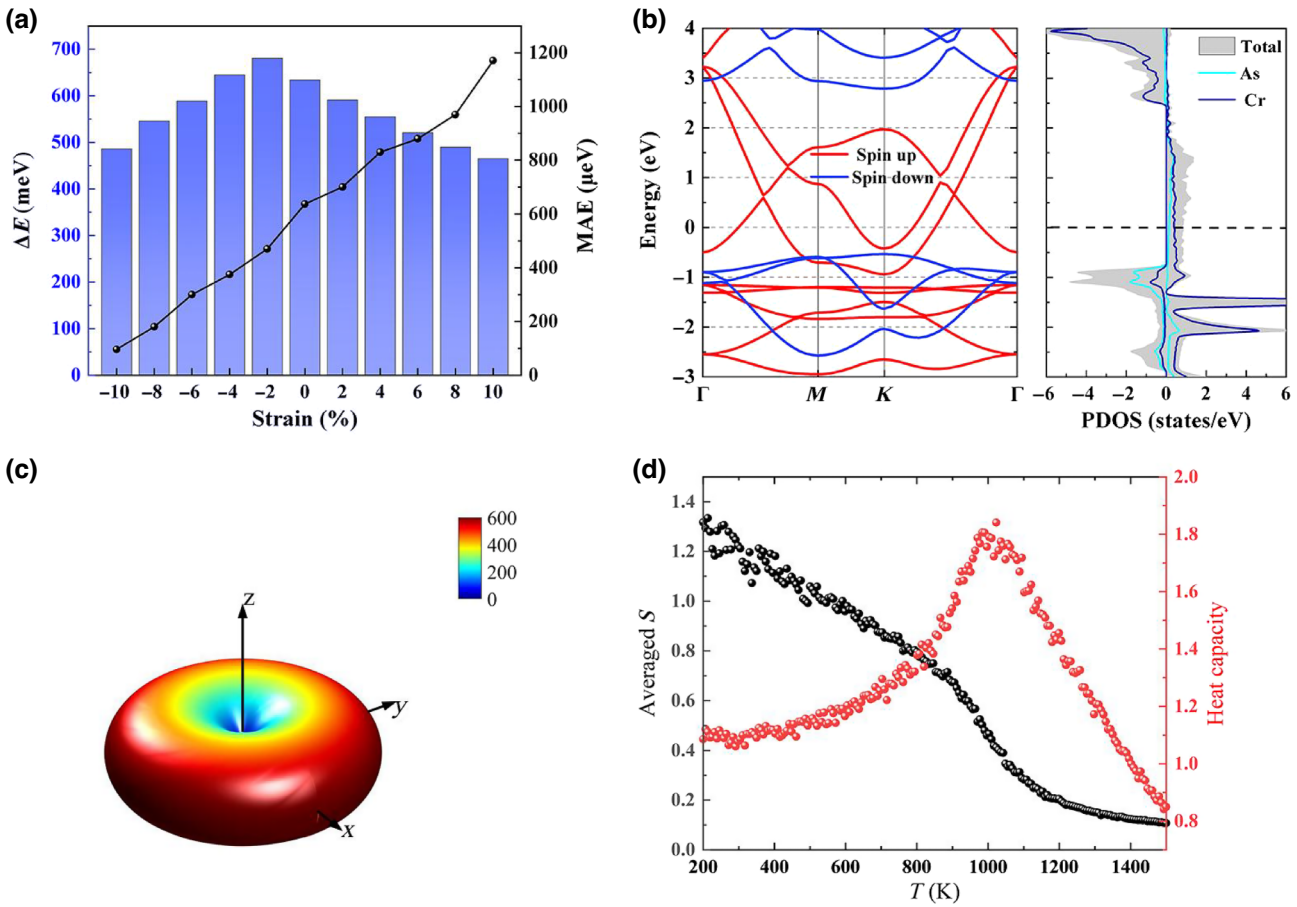
(a)

(b)

(c)

(d)

FIG. 2.   (a) The variation of ΔE and MAE under application of biaxial strain. (b) Band structures and PDOS for CrAs. (c) The spatial distribution of the MAE for CrAs under 0 strain. (d) Evolution of the specific heat capacity and averaged spin per Cr using Monte Carlo simulations.
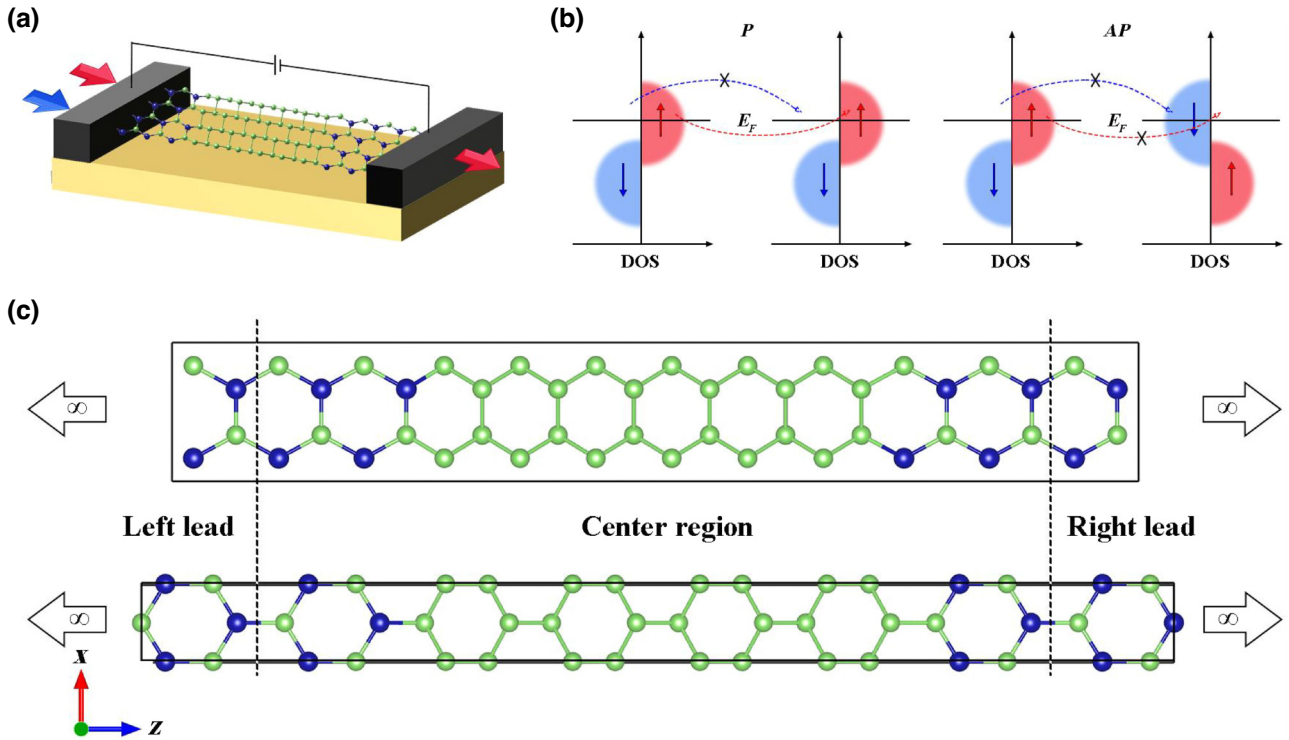
FIG. 3. (a) Schematic diagram of the tunnel magnetoresistance device based on monolayer CrAs. (b) The principle of the TMR effect of half-metal. (c) Schematic diagram of the CrAs/arsenene/CrAs device along zigzag (top) and armchair (bottom) directions.

destroyed by this physical adsorption process because it lacks orbital hybridization and charge transformation. The calculated exfoliation energy of the CrAs monolayer

is $26 \, \text{meV}/\text{Å}^2$, between graphene and h-BN monolayers ($21 \sim 28 \, \text{meV}/\text{Å}^2$) [62], such a moderate exfoliation energy of the CrAs monolayer provides a fairly typical
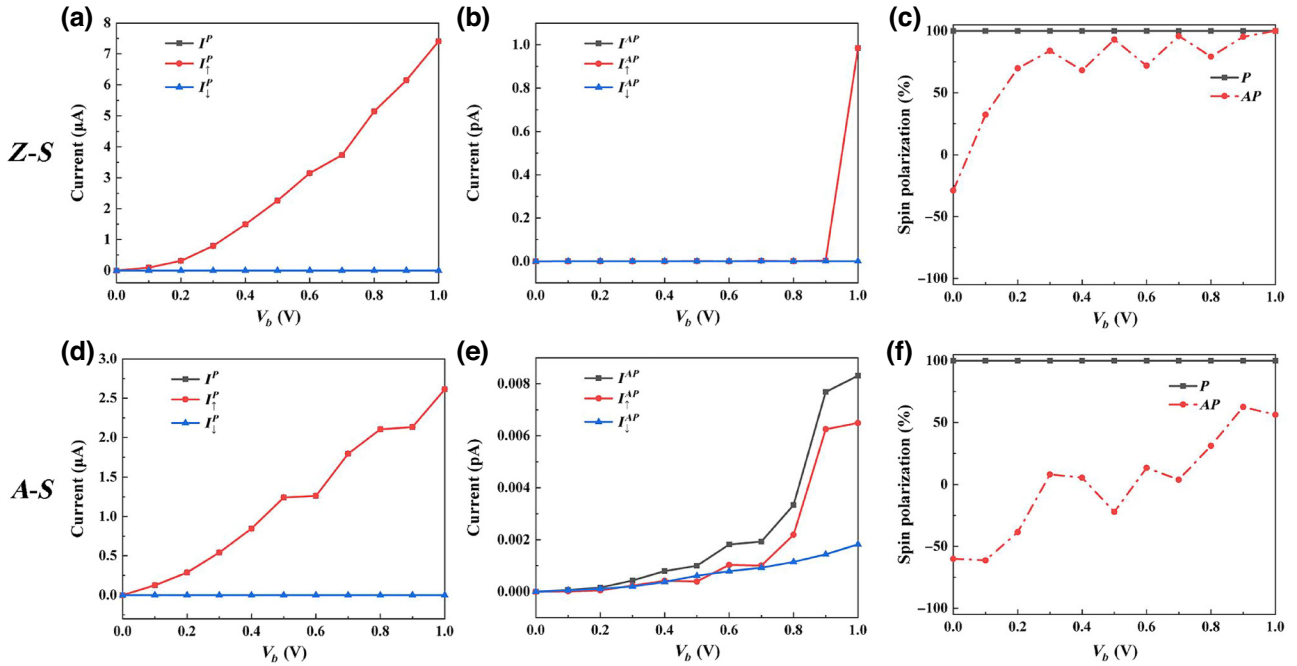

FIG. 4. Spin-polarized I-V curves and SPR for (a)–(c) Z-S and (d)–(f) A-S in the cases of PC and APC.
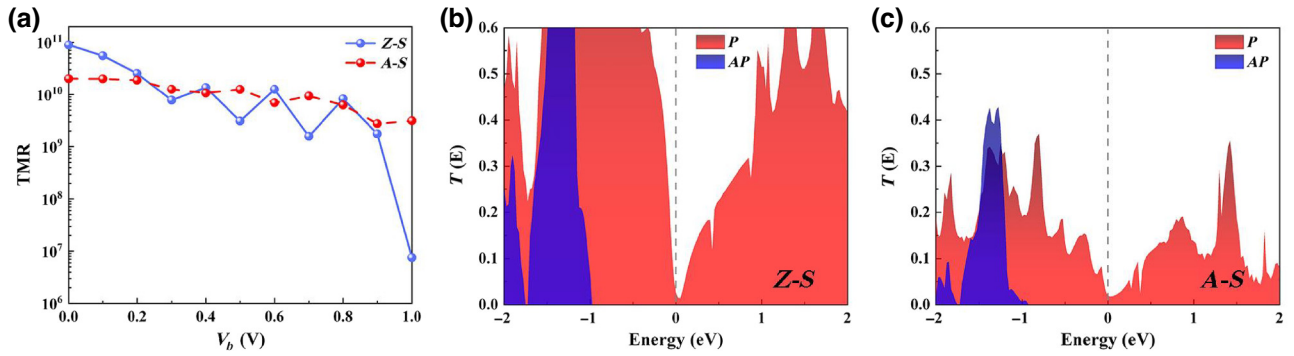
FIG. 5.   (a) TMR versus the bias voltage. Transmission function spectra of *Z-S* (b) and *A-S* (c) at the zero-bias for PC and APC.

2D material with moderate vdW interactions, implying the easy exfoliation from its multilayer materials. A non-magnetic semiconductor must be found for the center scattering zone of an MTJ constructed using CrAs as the electrode, and there should be as little lattice mismatch as possible between the electrode and the semiconductor. As a nonmagnetic semiconductor, buckled arsenene [63] has a lattice mismatch rate about 6.2% when combined with CrAs, and according to previous reports, buckled arsenene remains dynamically stable under approximately 18% tensile strain [64]. We construct two MTJs for ArCr/arsenene/CrAs along the zigzag and armchair directions: *Z* system (*Z-S*) and *A* system (*A-S*). The potential application about spin transport of a CrAs-based MTJ on an insulating substrate is shown in Fig. 3(a). As shown in Fig. 3(c), CrAs and arsenene layers make up the central scattering area, whereas infinite CrAs magnetic layers make up the left and right leads. When bias voltages are applied, electrons can be transported along the *z* axis.

Figure 4 shows the results of calculating the tunneling currents that rely on bias (*I-V*) in PC and APC along the *Z-S* and *A-S*, respectively. The use of half-metallic materials as leads causes the spin-up tunneling current to be much larger than the spin-down current for both devices. In both devices, the tunneling currents in the PC are much larger than in the APC. Moreover, in both *Z-S* and *A-S*, the detected currents in the devices reached the μA level under PC. Because the currents are of such high order of magnitude, the currents produced in such MTJs are all detectable in the experiment. The corresponding SPRs for different configurations are presented in Figs. 4(c) and 4(f). It can be observed that under PC, for *Z-S* and *A-S*, the spin-down current can be ignored in favor of the spin-up current since the $I_\uparrow^P$ values rise quickly whereas $I_\downarrow^P$ are limited through the complete bias-voltage range, producing the almost perfect spin-filtering effect with SPR^P approximately equals to 100%. For APC under equilibrium, the SPR^{AP} of both MTJs is negative, and the
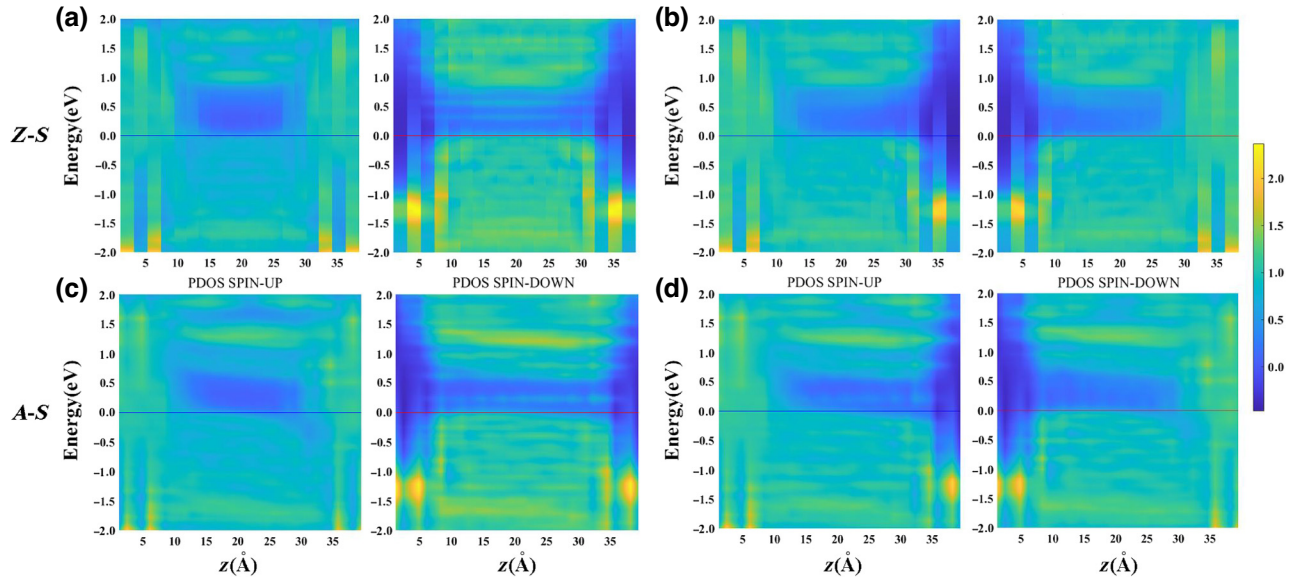

FIG. 6.   Spin-resolved PDOS of the *Z-S* in the (a) PC and (b) APC states as well as the *A-S* in the (c) PC and (d) APC states.
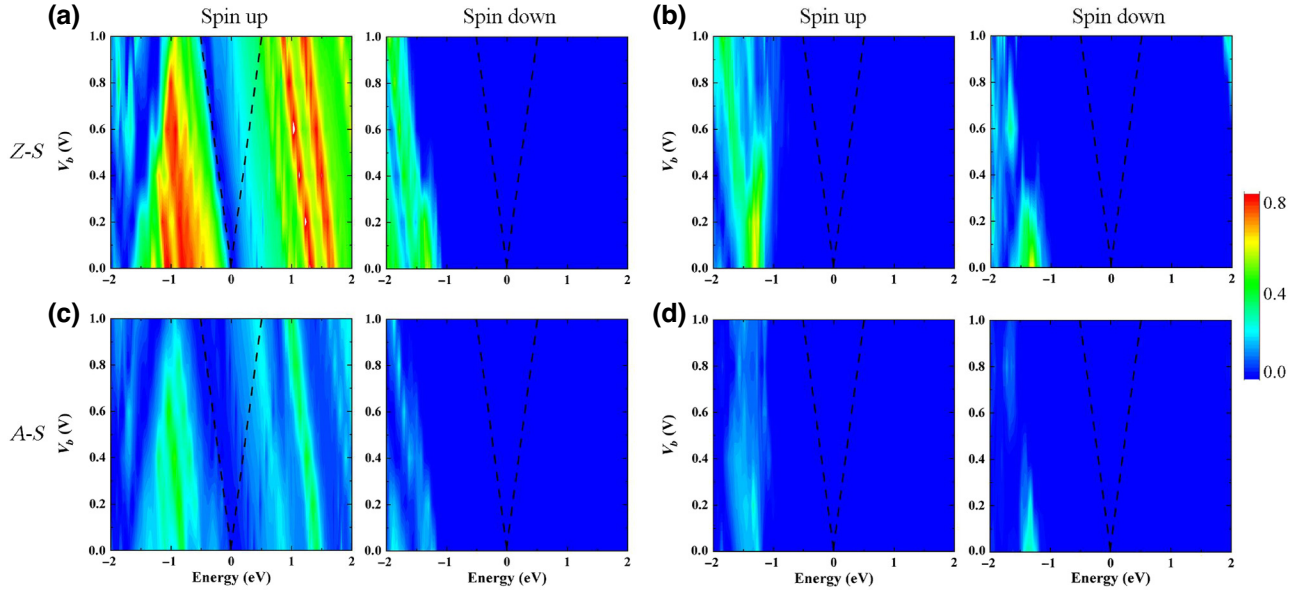
FIG. 7. Different-spin transmission function spectra for PC and APC. (a),(b) Transmission function spectra of *Z-S* for PC and APC. (c),(d) Corresponding results of *A-S*. Black dash lines indicate the bias window.

SPR^{AP} increases as the bias increases. For *Z-S*, it increases rapidly and oscillates around 100%, while *A-S* cannot get a good spin-filtering effect.

Based on the total currents I^P and I^{AP}, the TMR ratio was determined using Eq. (4). Both devices have a significant TMR ratio due to the large tunneling current differential between the APC and PC. The calculated TMR ratio values as a function of bias voltage, presented in Fig. 5(a), indicates that the *Z-S* device at a maximum TMR ratio reaches 10^{10}, and the minimum is still close to 10^7. The TMR of *A-S* remains at 10^{10} over the whole bias-voltage range. In Figs. 5(b) and 5(c), we provide the transmission function curves at zero bias voltage, which are expressed as $T(E) = \sum_\sigma T_\sigma(E)$. This finding makes it easier to comprehend why TMR levels are so high. Near the Fermi level, T^P for PC approaches 0.1 for *Z-S* and *A-S*, but T^{AP} approximately equals to 0 in the APC. This implies that electrons pass across MTJs much more readily in PC but much more difficultly in APC. As a result, the TMR values associated with *Z-S* and *A-S* are significantly high.

To demonstrate the spin-dependent transport characteristics, the projected density of states (PDOS) along the transport direction is determined (Fig. 6). It is evident that the electrode region of the device in PC exhibits a notably elevated DOS distribution in CrAs, which suggests a marked metallization of the electrode region. A band gap is present in the center scattering region, which is blue in the middle. Because the region of central scattering consists of a semiconductor, there is a visible potential

barrier in PDOS that limits the flow of electrons. In addition, the spin-up channels exhibit much bigger MTJ states compared to the spin-down channels, indicating a distinct spin-filtering effect. For the APC, where the spin-up (spin-down) electrons flow from the left CrAs into the arsenene with majority (minority) states and out through the right CrAs near the Fermi level. A higher DOS is observed just on one side of the electrode region. This is because, the device's magnetization is in the opposite direction, which restricts electron transport. Therefore, a high resistance state in the MTJ is provided by CrAs opposing states to the left and right of arsenene.

To provide a more comprehensive understanding of the mechanisms behind the spin-dependent transport properties of CrAs-based MTJs, we propose to describe the transmission function in terms of bias voltage and energy. The regions delineated by dashed lines in Fig. 7 represent bias-induced Fermi-window boundaries. Only the projection peak in the bias window contributes to the device current, which relies on the transmission peak area. In the PC, the significant transmission function magnitude in the Fermi window is usually accompanied with spin-up transmission peaks. Rather, there is a severe suppression of all spin-down transmission peaks. As a result, during the whole Fermi window, $I_\uparrow^P$ is bigger than $I_\downarrow^P$, thus the SPR stays almost at 100% [see Figs. 7(a) and 7(c)]. In the APC, the Fermi window shows no transmission peaks. So under this case, electron transmission is severely inhibited. This is the reason why the TMR of the CrAs/arsenene/CrAs device can reach the order of 10^{10}.

IV. SUMMARY

In summary, first-principles and NEGF analyses are used to thoroughly investigate the electronic structures, magnetic and spin-dependent transport features of CrAs. Research has shown that CrAs has a high Curie temperature and is an out-of-plane FM half-metal. Moreover, the out-of-plane FM ground state is discovered to be robust to biaxial strain. The spacer region was filled with semiconductor arsenene, while the half-metallic CrAs monolayer was considered as magnetic electrodes. Significantly high SPR and TMR have been observed in the devices along zigzag or armchair directions. The maximum TMR of CrAs/arsenene/CrAs can almost reach 8.9×10^{10} and stays higher than 10^6 under bias voltages up to 1 V. Besides, given a value of SPR in PC reaching 100% with bias, the MTJs prove a remarkable single spin-filtering effect. Through the examination of the PDOS and transmission spectra, we can get a deeper comprehension of the potential processes behind spintronic phenomena. According to our research, the suggested MTJ could be an ideal choice for multifunctional spintronic devices.

ACKNOWLEDGMENTS

[1] Y. X. Zhang, L. D. Guo, X. W. Zhu, and X. N. Sun, The application of organic semiconductor materials in spintronics, Front. Chem. **8**, 589207 (2020).

[2] G. Serrano, E. Velez-Fort, I. Cimatti, B. Cortigiani, and R. Sessoli, Magnetic bistability of a TbPc$_2$ submonolayer on a graphene/SiC(0001) conductive electrode, Nanoscale **10**, 2715 (2018).

[3] D. Wang, Z. W. Wang, N. U. Xu, L. Liu, and G. Z. Xing, Synergy of spin-orbit torque and built-in field in magnetic tunnel junctions with tilted magnetic anisotropy: Toward tunable and reliable spintronic neurons, Adv. Sci. **9**, 2203006 (2022).

[4] A. Sengupta, A. Banerjee, and K. Roy, Hybrid spintronic-CMOS spiking neural network with on-chip learning: Devices, circuits, and systems, Phys. Rev. Appl. **6**, 064003 (2016).

[5] S. Yang, S. Park, and J. Bintinger, Employing pneumatic nozzle printing for controlling the crystal growth of small molecule organic semiconductor for field-effect transistors, Adv. Electron. Mater. **4**, 1700534 (2018).

[6] M. Houssa and K. Iordanidou, Point defects in MoS$_2$: Comparison between first-principles simulations and electron spin resonance experiments, Appl. Surf. Sci. **416**, 853 (2017).

[7] B. P. Yalagala, A. S. Dahiya, and R. Dahiya, ZnO nanowires based degradable high-performance photodetectors for eco-friendly green electronics, Opto-Electron. Adv. **6**, 220020 (2023).

[8] J. C. D. dos Santos, D. F. S. Ferreira, C. A. B. da Silva, and J. Del Nero, Transitions in electrical behavior of Molecular Devices based on 1-D and 2-D graphene-phagraphene-graphene hybrid heterojunctions, Mater. Chem. Phys. **253**, 123420 (2020).

[9] A. Banerjee, B. Kundu, and A. J. Pal, Introducing immobilized metal phthalocyanines as spin-injection and detection layers in organic spin-valves: Spin-tunneling and spin-transport regimes, Org. Electron. **41**, 173 (2017).

[10] D. Cakir, D. M. Otalvaro, and G. Brocks, From spin-polarized interfaces to giant magnetoresistance in organic spin valves, Phys. Rev. B **89**, 115407 (2014).

[11] Y. W. Yin, X. Y. Jiang, M. A. Koten, and J. E. Shield, Spin rectification and electrically controlled spin transport in molecular-ferroelectrics-based spin valves, Phys. Rev. Appl. **13**, 064011 (2020).

[12] X. M. Zhang, J. W. Tong, L. X. Ruan, and G. W. Qin, Interface hybridization and spin filter effect in metal-free phthalocyanine spin valves, Phys. Chem. Chem. Phys. **22**, 11663 (2020).

[13] M. Luo, Antiferromagnetic spin valve based on a heterostructure of two-dimensional hexagonal crystals, Phys. Rev. B **99**, 165407 (2019).

[14] P. N. Abufager, R. Robles, and N. Lorente, FeCoCp$_3$ molecular magnets as spin filters, J. Phys. Chem. C **119**, 12119 (2015).

[15] F. F. Li and J. Huang, Spin-transport tuning of individual magnetic Mn-salophen molecule via chemical adsorption, Molecules **24**, 1747 (2019).

[16] F. X. Zu, G. Y. Gao, and H. H. Fu, Efficient spin filter and spin valve in a single-molecule magnet Fe4 between two graphene electrodes, Appl. Phys. Lett. **107**, 252403 (2015).

[17] Z. Z. Lin and X. Chen, Ultrathin scattering spin filter and magnetic tunnel junction implemented by ferromagnetic 2D van der Waals material, Adv. Electron. Mater. **6**, 1900968 (2020).

[18] P. H. Li, Y. J. Chen, B. Y. Wang, M. M. Li, D. Xiang, C. C. Jia, and X. F. Guo, Single-molecule optoelectronic devices: Physical mechanism and beyond, Opto-Electron. Adv. **5**, 210094 (2022).

[19] E. M. Chudnovsky, Quantum tunneling of the magnetic moment in the S/F/S Josephson phi(0) junction, Phys. Rev. B **93**, 144422 (2016).

[20] W. Yan, X. F. Han, and X. G. Zhang, Effect of Co interlayers in Fe/MgO/Fe magnetic tunnel junctions, Appl. Phys. Lett. **93**, 172501 (2008).

[21] J. Li and L. C. Xu, The transport and optoelectronic properties of gamma-graphyne-based molecular magnetic tunnel junctions, Carbon **132**, 632 (2018).

[22] Y. Q. Ke, X. Ke, and H. Guo, Oxygen-vacancy-induced diffusive scattering in Fe/MgO/Fe magnetic tunnel junctions, Phys. Rev. Lett. **105**, 236801 (2010).

[23] C. Chao, Y. Wang, and H. P. Cheng, Perfect spin-filtering and giant magnetoresistance with Fe-terminated graphene nanoribbon, Appl. Phys. Lett. **99**, 073110 (2011).

[24] M. Y. Di, Z. Yang, and J. Li, The spin-dependent transport and optoelectronic properties of the 6,6,12-graphyne-based

magnetic tunnel junction devices, Org. Electron. **53,** 1 (2017).

[25] A. Aadhityan, C. P. Kala, and D. J. Thiruvadigal, First principle study on TMR effect in A-MgO-A (A = Fe, Co and Ni) magnetic tunnel junction, Appl. Surf. Sci. **449,** 799 (2017).

[26] T. C. Song, X. H. Cai, M. W. Y. Tu, X. O. Zhang, B. V. Huang, and N. P. Wilson, Giant tunneling magnetoresistance in spin-filter van der Waals heterostructures, Science **360,** 1214 (2018).

[27] J. S. Moodera and L. R. Kinder, Ferromagnetic-insulator-ferromagnetic tunneling: Spin-dependent tunneling and large magnetoresistance in trilayer junctions, J. Appl. Phys. **79,** 4724 (1996).

[28] N. N. Beletskii, G. P. Berman, A. R. Bishop, and V. M. Yakovenko, Magnetoresistance and spin polarization of electron current in magnetic tunnel junctions, Phys. Rev. B **75,** 174418 (2007).

[29] X. J. Liu, T. J. Wang, L. Niu, Y. Wang, Q. Zhang, and H. T. Yin, Magnetic proximity, magnetoresistance and spin filtering effect in a binuclear ferric phthalocyanine from first principles, J. Phys. D **53,** 035305 (2020).

[30] B. Wang and J. W. Li, Giant tunnel magneto-resistance in graphene-based molecular tunneling tunction, Nanoscale **8,** 3432 (2016).

[31] T. Ohta, A. Bostwick, and T. Seyller, Controlling the electronic structure of bilayer graphene, Science **313,** 951 (2006).

[32] S. Q. Yan, Y. Zuo, S. S. Xiao, L. K. Oxenlowe, and Y. H. Ding, Graphene photodetector employing double slot structure with enhanced responsivity and large bandwidth, Opto-Electron. Adv. **5,** 210159 (2022).

[33] Q. X. Pei, X. L. Zhang, Z. W. Ding, Y. Y. Zhang, and Y. W. Zhang, Thermal stability and thermal conductivity of phosphorene in phosphorene/graphene van der Waals heterostructures, Phys. Chem. Chem. Phys. **19,** 17180 (2017).

[34] B. Zhang, L. H. Zhang, and J. Y. Zhang, Cross structured two-dimensional violet phosphorene with extremely high deformation resistance, J. Mater. Chem. A **9,** 13855 (2021).

[35] Y. D. Wang, Y. W. Wang, Y. L. Dong, L. Zhou, J. L. Kang, N. Wang, Y. J. Li, X. M. Yuan, Z. W. Zhang, H. Huang, M. Q. Long, S. Xiao, and J. He, 2D Nb$_2$CT$_x$ MXene/MoS$_2$ heterostructure construction for nonlinear optical absorption modulation, Opto-Electron. Adv. **6,** 220162 (2023).

[36] J. F. Ping, Z. X. Fan, M. Sindoro, Y. B. Ying, and H. Zhang, Recent advances in sensing applications of two-dimensional transition metal dichalcogenide nanosheets and their composites, Adv. Funct. Mater. **27,** 1605817 (2017).

[37] M. Shahzadi, C. Y. Zheng, S. Ahmad, S. S. Wang, and W. L. Zhang, Exciton-polariton based WS$_2$ polarization modulator controlled by optical Stark beam, Opto-Electron. Adv. **5,** 200066 (2022).

[38] J. H. Min, K. Lee, T. H. Chung, J. W. Min, K. H. Li *et al.* Large-scale and high-quality III-nitride membranes through microcavity-assisted crack propagation by engineering tensile-stressed Ni layers, Opto-Electron. Sci. **1,** 220016 (2022).

[39] H. Zhao, X. K. Wang, S. T. Liu, and Y. Zhang, Highly efficient vectorial field manipulation using a transmitted tri-layer metasurface in the terahertz band, Opto-Electron. Adv. **6,** 220012 (2023).

[40] P. L. Hong, L. Xu, and M. Rahmani, Dual bound states in the continuum enhanced second harmonic generation with transition metal dichalcogenides monolayer, Opto-Electron. Adv. **5,** 200097 (2022).

[41] K. R. Li, T. H. Chang, and P. Y. Chen, Tunable magnetic response in 2D materials via reversible intercalation of paramagnetic ions, Adv. Electron. Mater. **5,** 1900040 (2019).

[42] H. Wang, X. Y. Li, and J. He, Two-dimensional ferromagnetic materials: From materials to devices, Appl. Phys. Lett. **121,** 220501 (2022).

[43] S. N. Reed-Lingenfelter, M. J. Wang, N. L. Williams, and J. J. Cha, Surface functionalization for magnetic property tuning of nonmagnetic 2D materials, Adv. Mater. Interfaces **9,** 2100463 (2022).

[44] C. Y. Dai, P. He, and J. Zheng, Research progress of two-dimensional magnetic materials, Sci. China Mater. **66,** 859 (2023).

[45] Y. Y. Yao, X. Y. Zhan, and J. He, Recent progress on emergent two-dimensional magnets and heterostructures, Nanotechnology **32,** 472001 (2021).

[46] Y. L. Feng, N. Liu, and G. Y. Gao, Spin transport properties in Dirac spin gapless semiconductors Cr$_2$X$_3$ with high Curie temperature and large magnetic anisotropic energy, Appl. Phys. Lett. **118,** 112407 (2021).

[47] X. L. Zhang, P. W. Gong, F. Q. Liu, J. Wu, and S. C. Zhu, Mn$_2$NT$_2$ (T = O, F) nanosheets for electrically and thermally driven magnetic tunnel junctions, ACS Appl. Nano Mater. **5,** 15183 (2022).

[48] Q. Ma, W. Wan, Y. Li, and Y. Liu, First principles study of 2D half-metallic ferromagnetism in Janus Mn$_2$XSb (X = As, P) monolayers, Appl. Phys. Lett. **120,** 112402 (2022).

[49] H. Xiao, X. Wang, R. Wang, L. Xu, S. Liang, and C. Yang, Intrinsic magnetism and biaxial strain tuning in two-dimensional metal halides V$_3$X$_8$ (X = F, Cl, Br, I) from first principles and Monte Carlo simulation, Phys. Chem. Chem. Phys. **21,** 11731 (2019).

[50] G. Xiao, W. Z. Xiao, Y. X. Feng, Q. Y. Rong, and Q. Chen, Two-dimensional ferroelastic and ferromagnetic NiOX (X = Cl and Br) with half-metallicity and a high Curie temperature, Nanoscale **15,** 17963 (2023).

[51] G. Rahman and Z. Jahangirli, CrAs Monolayer: Low buckled 2D half-metal ferromagnet, Phys. Status Solidi RRL **14,** 1900509 (2020).

[52] G. Kresse and J. Furthmüller, Efficiency of ab-initio total energy calculations for metals and semiconductors using a plane-wave basis set, Comput. Mater. Sci. **6,** 15 (1996).

[53] G. Kresse and D. Joubert, From ultrasoft pseudopotentials to the projector augmented-wave method, Phys. Rev. B **59,** 1758 (1999).

[54] J. P. Perdew, K. Burke, and M. Ernzerhof, Generalized gradient approximation made simple, Phys. Rev. Lett. **77,** 3865 (1996).

[55] A. V. Kuklin, A. A. Kuzubov, E. A. Kovaleva, N. S. Mikhaleva, F. N. Tomilin, H. Lee, and P. V. Avramov, Two-dimensional hexagonal CrN with promising magnetic and optical properties: A theoretical prediction, Nanoscale **9,** 621 (2017).

[56] J. Taylor, H. Guo, and J. Wang, Ab initio modeling of quantum transport properties of molecular electronic devices, Phys. Rev. B **63,** 245407 (2001).

[57] D. Waldron and P. Haney, Nonlinear spin current and magnetoresistance of molecular tunnel junctions, Phys. Rev. Lett. **96,** 166804 (2006).

[58] A. R. Rocha, V. M. Garcia-Suarez, and S. Bailey, Spin and molecular electronics in atomically generated orbital landscapes, Phys. Rev. B **73,** 085414 (2006).

[59] L. M. Cao, X. B. Li, C. X. Jia, G. Liu, Z. R. Liu, and G. H. Zhou, Spin-charge transport properties for graphene/graphyne zigzag-edged nanoribbon heterojunctions: A first-principles study, Carbon **127,** 519 (2018).

[60] M. Büttiker, Y. Imry, R. Landauer, and S. Pinhas, Generalized many-channel conductance formula with application to small rings, Phys. Rev. B **31,** 6207 (1985).

[61] A. Togo and I. Tanaka, First principles phonon calculations in materials science, Scr. Mater. **108,** 1 (2015).

[62] J. H. Jung, C. H. Park, and J. Ihm, A Rigorous method of calculating exfoliation energies from first principles, Nano Lett. **18,** 2759 (2018).

[63] C. Kamal and M. Ezawa, Arsenene: Two-dimensional buckled and puckered honeycomb arsenic systems, Phys. Rev. B **91,** 085423 (2015).

[64] G. Rahman, A. Mahmood, and V.M. García-Suárez, Dynamically stable topological phase of arsenene, Sci. Rep. **9,** 7966 (2019).